



**HAL**  
open science

## **Actinide Coordination Chemistry on Surfaces: Synthesis, Manipulation, and Properties of Thorium Bis(porphyrinato) Complexes**

Erik Rheinfrank, Mathias Pörtner, Maria del Carmen Nuñez Beyerle, Felix Haag, Peter S Deimel, Francesco Allegretti, Knud Seufert, Johannes V Barth, Marie-Laure Bocquet, Peter Feulner, et al.

### ► To cite this version:

Erik Rheinfrank, Mathias Pörtner, Maria del Carmen Nuñez Beyerle, Felix Haag, Peter S Deimel, et al.. Actinide Coordination Chemistry on Surfaces: Synthesis, Manipulation, and Properties of Thorium Bis(porphyrinato) Complexes. *Journal of the American Chemical Society*, 2021, 143 (36), pp.14581-14591. <10.1021/jacs.1c04982>. <hal-03432277>

**HAL Id: hal-03432277**

**<https://hal.science/hal-03432277v1>**

Submitted on 17 Nov 2021

HAL is a multi-disciplinary open access archive for the deposit and dissemination of scientific research documents, whether they are published or not. The documents may come from teaching and research institutions in France or abroad, or from public or private research centers.

L'archive ouverte pluridisciplinaire HAL, est destinée au dépôt et à la diffusion de documents scientifiques de niveau recherche, publiés ou non, émanant des établissements d'enseignement et de recherche français ou étrangers, des laboratoires publics ou privés.



HAL Authorization

## 1 Actinide Coordination Chemistry on Surfaces: Synthesis, 2 Manipulation, and Properties of Thorium Bis(porphyrinato) 3 Complexes

4 Erik Rheinfrank, Mathias Pörtner, Maria del Carmen Nuñez Beyerle, Felix Haag, Peter S. Deimel,  
5 Francesco Allegretti, Knud Seufert, Johannes V. Barth, Marie-Laure Bocquet, Peter Feulner,  
6 and Willi Auwärter\*



Cite This: <https://doi.org/10.1021/jacs.1c04982>



Read Online

ACCESS |



Metrics & More

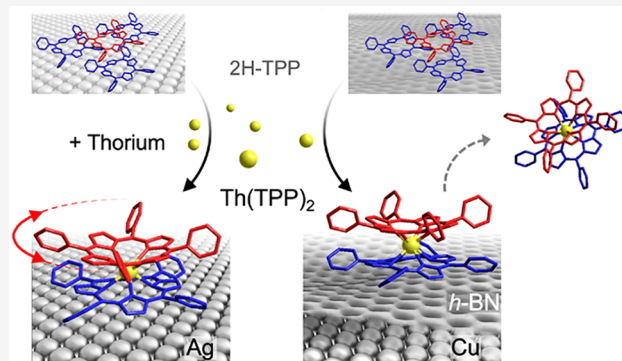


Article Recommendations



Supporting Information

7 **ABSTRACT:** Actinide-based metal–organic complexes and coordi-  
8 nation architectures encompass intriguing properties and function-  
9 alities but are still largely unexplored on surfaces. We introduce the  
10 in situ synthesis of actinide tetrapyrrole complexes under ultrahigh-  
11 vacuum conditions, on both a metallic support and a 2D material.  
12 Specifically, exposure of a tetraphenylporphyrin (TPP) multilayer to  
13 an elemental beam of thorium followed by a temperature-  
14 programmed reaction and desorption of surplus molecules yields  
15 bis(porphyrinato)thorium ( $\text{Th}(\text{TPP})_2$ ) assemblies on Ag(111) and  
16 hexagonal boron nitride/Cu(111). A multimethod characterization  
17 including X-ray photoelectron spectroscopy, scanning tunneling  
18 microscopy, temperature-programmed desorption, and complemen-  
19 tary density functional theory modeling provides insights into  
20 conformational and electronic properties. Supramolecular assemblies  
21 of  $\text{Th}(\text{TPP})_2$  as well as individual double-deckers are addressed with submolecular precision, e.g., demonstrating the reversible  
22 rotation of the top porphyrin in  $\text{Th}(\text{TPP})_2$  by molecular manipulation. Our findings thus demonstrate prospects for actinide-based  
23 functional nanoarchitectures.



### 24 ■ INTRODUCTION

25 Understanding the organometallic and coordination chemistry  
26 of actinide elements has drawn considerable interest in recent  
27 years.<sup>1–8</sup> High coordination numbers, a variety of available  
28 oxidation states, and the presence of 5f orbitals allow actinides  
29 to access reactivity modes and coordination environments that  
30 differ from the characteristics of d-block elements and  
31 lanthanides. As elemental metals, actinides are less homoge-  
32 neous than their 4f counterparts. Their 5f electrons are  
33 localized exclusively for the late members of the series from  
34 Am through Lr. The early actinides through Pu show, in  
35 contrast to all lanthanides, itinerant 5f electrons that take part  
36 in bonding and screening, causing a parabolic dependence of  
37 the Wigner–Seitz radii on the atomic numbers similar to d-  
38 block elements, 5f density of states (DOS) directly at the  
39 Fermi edge seen in ultraviolet photoelectron spectroscopy  
40 (UPS), and well-screened inner-shell vacancies in X-ray  
41 photoelectron spectroscopy (XPS) (see ref 9 and references  
42 therein). These volatile 5f electrons enable oxidation states up  
43 to +7 for Np.<sup>10</sup> Comparing compounds with corresponding  
44 lanthanide and actinide atoms, bonds with actinide partners are  
45 generally considered to show increased covalent versus ionic

character, whereas for the early group members Ce and Th, 46  
reversed results have been reported.<sup>11,12</sup> These properties, and 47  
the actinides' larger ionic radii that affect bond character and 48  
geometry, open prospects for novel functional materials, 49  
including single-molecule magnets<sup>13–15</sup> and coordination 50  
architectures, covering metal–organic coordination frame- 51  
works.<sup>16–18</sup> The latter structures are expected to play a 52  
relevant role in nuclear waste management.<sup>19</sup> Uranium- and 53  
thorium-based complexes and molecular materials have 54  
received the main attention, e.g., because of their interesting 55  
catalytic chemistry<sup>20–24</sup> and intriguing coordination structures 56  
reported.<sup>6,17,18,25–32</sup> Specifically, thorium tetrapyrrole com- 57  
plexes (including porphyrins, phthalocyanines, and corroles) 58  
were achieved,<sup>6,33–35</sup> affording double-decker bis- 59  
(porphyrinato)thorium complexes, where a single thorium 60

Received: May 13, 2021

61 center is sandwiched between two macrocyclic ligands.<sup>36–38</sup> In  
62 addition, the large half-lives of <sup>232</sup>Th (1.4 × 10<sup>10</sup> years) and  
63 <sup>238</sup>U (4.47 × 10<sup>9</sup> years) minimize radiation hazards compared  
64 to other, more short-lived actinides.

65 So far, most of this work on metal–organic actinide  
66 complexes has been carried out in solution or solid state.  
67 Single-molecule characterization, supramolecular assembly,  
68 and chemistry directly on surfaces remain unexplored—in  
69 stark contrast to the lanthanide counterparts (see below)—  
70 mainly because of safety restrictions due to radiation. Metal  
71 surfaces, however, provide excellent platforms to assemble and  
72 synthesize metal–organic complexes and functional molecular  
73 architectures and to control and monitor the structural,  
74 electronic, and magnetic properties under ultrahigh-vacuum  
75 (UHV) conditions.<sup>39–42</sup> Moreover, two-dimensional materials  
76 and ultrathin films can be used to reduce molecule–metal  
77 interactions that can adversely affect or mask intrinsic  
78 molecular properties, with a monolayer of insulating hexagonal  
79 boron nitride (*h*-BN) being a prominent example of such a  
80 decoupling layer.<sup>43,44</sup> Indeed, surface science experiments and  
81 complementary theoretical modeling have provided exciting  
82 insights into lanthanide-based tetrapyrrole complexes and  
83 coordination architectures on model surfaces,<sup>45</sup> with pioneer-  
84 ing studies on double-decker and multidecker structures,<sup>46–52</sup>  
85 including TbPc<sub>2</sub> as an exemplary single-ion molecular  
86 magnet.<sup>53–56</sup> Thin decoupling layers were applied to improve  
87 the stability of the magnetic properties<sup>51,55</sup> or to manipulate  
88 the charge state of lanthanide–tetrapyrrole double-deckers.<sup>50</sup>  
89 As a downside, the intact deposition of such complexes by  
90 sublimation in a UHV environment poses severe challenges,  
91 with thermally induced molecular fragmentation or modifica-  
92 tions often interfering with clean, homogeneous adsorbate  
93 structures,<sup>46,52,57</sup> even though molecular functionalization can  
94 favor successful deposition.<sup>49</sup> In situ synthesis of lanthanide  
95 tetrapyrrole double-deckers and multideckers was resorted to  
96 as a remedy and alternative, e.g., yielding Ce(TPP)<sub>2</sub>,  
97 Ce<sub>2</sub>(TPP)<sub>3</sub>,<sup>58</sup> Gd<sub>x-1</sub>Pc<sub>x</sub> (*x* = 1–5),<sup>59</sup> TbPc<sub>2</sub>, and Tb(tbu-  
98 Pc)<sub>2</sub><sup>60</sup> complexes directly on noble metal supports.

99 Here, we introduce the in situ synthesis of Th(TPP)<sub>2</sub> (see  
100 Figure 1a–c) in a solvent-free UHV environment on two  
101 distinctly different substrates, namely, Ag(111) and *h*-BN/  
102 Cu(111). Our work thus expands on-surface metalation  
103 protocols, which are well-established for 3d metals,<sup>61,62</sup> alkali  
104 metals,<sup>63</sup> nonmetals,<sup>64,65</sup> and lanthanides,<sup>58–60,66</sup> to the  
105 actinide series. Along with extending tetrapyrrole surface  
106 science,<sup>67,68</sup> this study provides a rare example of a successful  
107 reaction on *h*-BN.<sup>69–74</sup>

108 The in situ synthesis process, inspired by the pioneering  
109 studies on lanthanide metalation,<sup>45,58–60</sup> is schematically  
110 illustrated in Figure 1d and e. It encompasses three steps:  
111 (1) growth of a precursor multilayer of 2H-TPP molecules on  
112 the substrate of choice; (2) deposition of elemental Th at  
113 room temperature (rt); and (3) thermal annealing at 500 K for  
114 several minutes to desorb unreacted multilayer components.  
115 The *h*-BN monolayer is prepared by chemical vapor deposition  
116 prior to the deposition of the molecules.<sup>75</sup> As sketched in the  
117 bottom panels of Figure 1d and e, the emerging surface  
118 morphologies are different for the two supports (Ag(111),  
119 Figure 1d; *h*-BN/Cu(111), Figure 1e). Furthermore, *h*-BN  
120 enables desorption and detection of the reaction products. The  
121 resulting Th(TPP)<sub>2</sub> sandwich complexes were investigated  
122 using X-ray photoelectron spectroscopy (XPS), scanning  
123 tunneling microscopy (STM), scanning tunneling spectroscop-

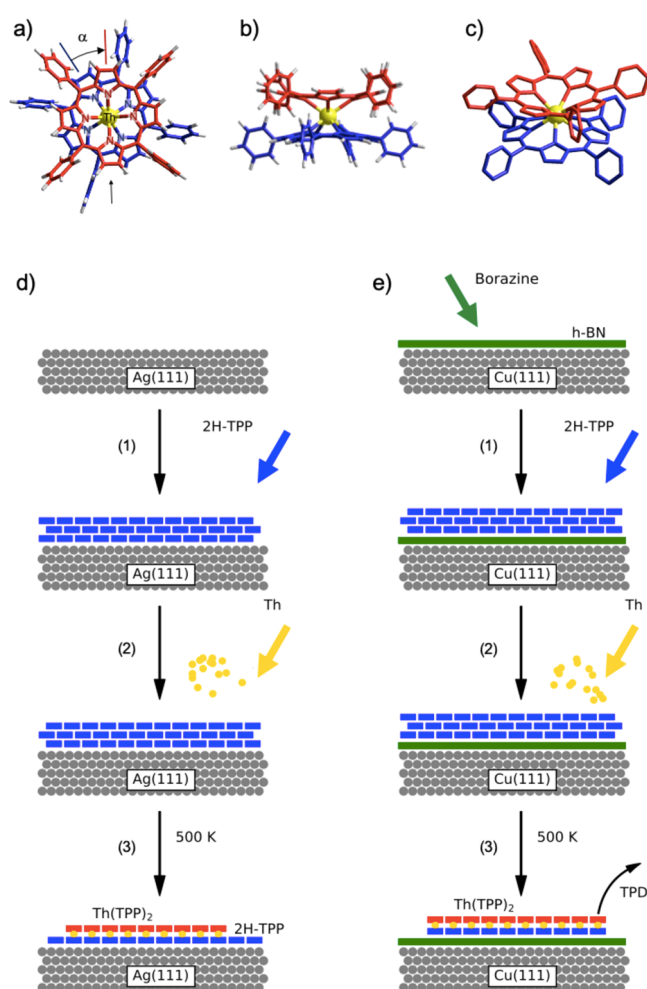


**Figure 1.** (a–c) DFT-optimized structure of a bis(porphyrinato)-thorium double-decker complex (Th(TPP)<sub>2</sub>) in vacuum. The two TPP units connected via the Th center (yellow) are colored in red and blue, respectively. (a) Top view.  $\alpha$  denotes the twist angle between the two macrocycles. (b) Side view (in the direction of the arrow in panel a). (c) 3D view (hydrogens omitted for clarity). (d, e) Schematic of the three-step synthesis route (1–3) for the formation of Th(TPP)<sub>2</sub> on Ag(111) (d) and *h*-BN/Cu(111) (e). See text for details.

py (STS), and temperature-programmed desorption (TPD).  
124 On both supports, regular Th(TPP)<sub>2</sub> arrays are observed  
125 without a discernible difference in packing and molecular  
126 appearance. However, the electronic structure represented in  
127 dI/dV spectra reveals distinct differences, e.g., featuring a larger  
128 apparent electronic gap on *h*-BN/Cu(111). The twist angles  
129 between the two macrocyclic ligands were determined for  
130 Th(TPP)<sub>2</sub>/Ag(111) and hint to a deviation from a perfect  
131 square antiprismatic coordination of the Th center. Comple-  
132 mentary density functional theory (DFT) modeling reveals  
133 details of the molecular conformation, e.g., demonstrating an  
134 inverted dome shape of the upper TPP. Molecular  
135 manipulation applied to individual Th(TPP)<sub>2</sub> units anchored  
136 in a 2H-TPP layer induced the reversible rotation of the top  
137 porphyrin, thus demonstrating basic properties of a molecular  
138 rotational switch.<sup>76</sup> To this end, the large size of the Th center  
139 (ionic radius exceeding, e.g., the one of Tb)<sup>77</sup> might be  
140 instrumental in providing well-distanced macrocycles. 141

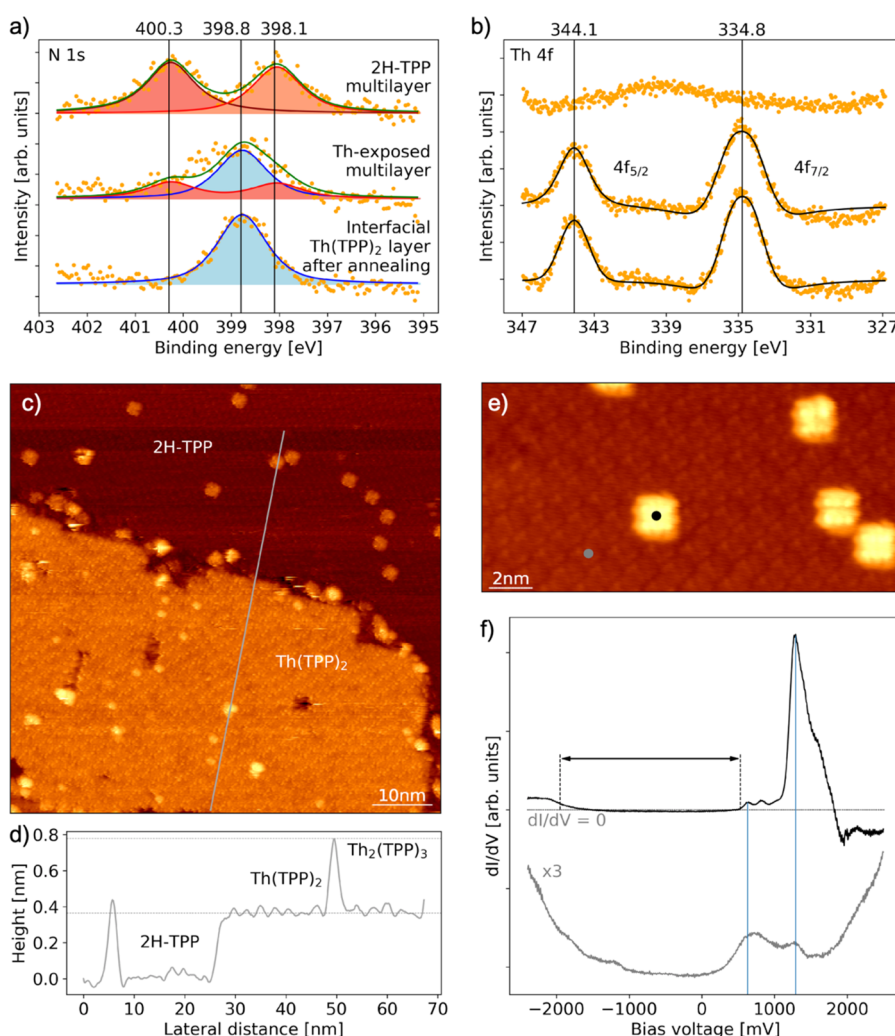


**Figure 2.** (a) Series of N 1s XP spectra representing a 2H-TPP multilayer on Ag(111) (top panel), the multilayer exposed to Th at rt (middle panel), and the resulting interfacial layer after thermal desorption of unreacted multilayer species (bottom panel). For each spectrum, fits are included for the individual components (see text for discussion). The respective binding energies are marked by the vertical lines with the values specified in eV. The maximum intensities of the spectra are normalized for better comparability. (b) Series of spin-orbit split Th 4f spectra representing the three synthesis steps described in panel a. (c) STM image of a Th(PPP)<sub>2</sub> island in a 2H-TPP array embedding individual Th(PPP)<sub>2</sub> units. (d) Apparent height profile along the path marked by the gray line in panel c. (e) Close-up STM image of individual Th(PPP)<sub>2</sub> in the 2H-TPP layer. The colored dots represent positions where dI/dV spectra were recorded (see panel f). (f) (Top panel) Characteristic dI/dV spectrum of Th(PPP)<sub>2</sub> revealing a large gap (marked by the arrow) and pronounced spectral features (see text for discussion). (Bottom panel) dI/dV reference spectrum of 2H-TPP. Tip stabilized at  $I_t = 60$  pA and  $V_b = 2.5$  V. Scanning conditions: (c)  $I_t = 0.7$  nA,  $V_b = 1.7$  V; (d)  $I_t = 0.7$  nA,  $V_b = 1.7$  V.

## 142 ■ RESULTS AND DISCUSSION

### 143 Thorium Bis(porphyrinato) Complexes on Ag(111).

144 The formation of Th(PPP)<sub>2</sub> complexes on Ag(111) was  
 145 monitored by XPS, following each step of the synthesis  
 146 process. The corresponding N 1s and Th 4f signatures  
 147 including fits are shown in parts a and b of Figure 2,  
 148 respectively. The evolution of the N 1s core-level spectrum  
 149 clearly reflected the metalation of the TPP. Before the  
 150 deposition of Th (Figure 2a, top panel), two separate peaks  
 151 arose from the two inequivalent nitrogen atoms in 2H-TPP,  
 152 i.e., the pyrrolic (–NH–) and iminic (–C=N–) species.<sup>78</sup>  
 153 The binding energies ( $E_b = 400.3$  and  $398.1$  eV) matched the  
 154 reported values for 2H-TPP multilayers on Ag(111) ( $400.2$   
 155 and  $398.1$  eV).<sup>79</sup> After dosing Th, the N 1s signature changed  
 156 considerably (Figure 2a, middle panel), reflecting a super-  
 157 position of signals from unreacted 2H-TPP and a new species  
 158 tentatively assigned to Th-metalated TPP. Following annealing

to 500 K, the width of the spectral feature was clearly reduced,  
 159 and the signal could be described by a main peak at  $E_b = 398.8$   
 160 eV (Figure 2a, bottom panel). This indicates the desorption of  
 161 unreacted TPP multilayer components and a dominating  
 162 contribution of metalated TPP, where all four nitrogen atoms  
 163 in the macrocycle are chemically equivalent. Such behavior is  
 164 well-known from the in situ metalation of tetrapyrroles<sup>61,62,78</sup>  
 165 and consistent with the formation of Th(PPP)<sub>2</sub> complexes.  
 166 The resulting N 1s binding energy compares well with values  
 167 reported for Fe-TPP ( $398.7$  eV<sup>79</sup> and  $398.4$  eV<sup>80</sup>), Ti-TPP  
 168 ( $398.6$  eV<sup>81</sup>), Ru-TPP ( $398.6$  eV<sup>82</sup>), and Co-TPP ( $398.8$   
 169 eV<sup>78</sup>) on Ag(111). However, it is considerably larger than the  
 170 N 1s binding energy ( $398.1$  eV) attributed to the N–Tb  
 171 component in TbPc<sub>2</sub> double-deckers on Ag(111).<sup>60</sup> Figure 2b  
 172 depicts the Th 4f<sub>7/2</sub> and 4f<sub>5/2</sub> core levels that exhibit strong  
 173 spin-orbit splitting. The binding energies (see Figure 2b)  
 174 match the ones reported for oxidized Th (ThO<sub>2</sub>,  $E_b = 344.2$   
 175

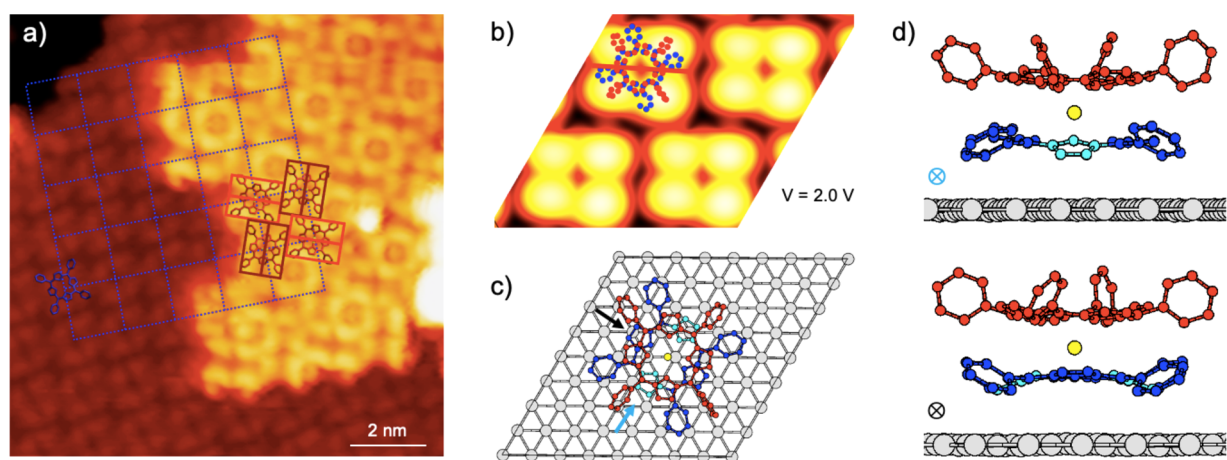


**Figure 3.** (a) STM image of a Th(TPP)<sub>2</sub> island embedded in a 2H-TPP array revealing submolecular contrast. The Th(TPP)<sub>2</sub> centers are in registry with the surrounding dense-packed 2H-TPP lattice (blue grid). The orientations of the upper porphyrin in adjacent Th(TPP)<sub>2</sub> units differ by  $\sim 90^\circ$ , as indicated by the molecular models framed in two shades of red. The main axis of the top ligand is marked by a line. A comparison to 2H-TPP (blue model) reveals a rotation of the upper porphyrin in Th(TPP)<sub>2</sub> by  $(33 \pm 6)^\circ$  or  $(-56 \pm 6)^\circ$  with respect to the bottom one. Scanning conditions:  $I_t = 0.1$  nA,  $V_b = 2.0$  V. (b) STM image simulation based on the DFT-optimized structure of Th(TPP)<sub>2</sub>/Ag(111) (see panels c and d) computed at 2 V bias voltage. (c, d) Structural model with top ligand, bottom ligand, Th center, and Ag surface colored in red, blue, yellow, and light gray, respectively. (c) Top view. The  $\kappa$ -pyrroles are highlighted in turquoise. (d) Side views in the two directions indicated by the colored arrows in panel c. Hydrogens are omitted for clarity.

176 and 334.9 eV) rather than the ones of the pure metal species  
177 ( $E_b = 342.4$  and 333.1 eV).<sup>83</sup> This finding shows that the Th is  
178 incorporated into the porphyrin's macrocycle and consistent  
179 with a Th oxidation state +IV, as expected for Th(TPP)<sub>2</sub>  
180 complexes.<sup>35</sup>

181 Because the XPS experiments point to a successful synthesis  
182 of Th(TPP)<sub>2</sub>, STM measurements were performed to get  
183 insight into the surface morphology of the resulting system.  
184 Figure 2c shows an STM image recorded after applying the  
185 synthesis procedure described earlier using a low Th dose. The  
186 silver surface was completely covered by well-ordered  
187 molecular arrays. The top part was identified as a 2H-TPP  
188 monolayer. The bottom part featured a compact island with an  
189 apparent height exceeding the surrounding 2H-TPP film.  
190 Because only a homogeneous monolayer and no second layer  
191 species were observed after annealing the 2H-TPP multilayer  
192 without the addition of Th,<sup>58</sup> this island was assigned to  
193 Th(TPP)<sub>2</sub>. Both the 2H-TPP layer and the Th(TPP)<sub>2</sub> array  
194 hosted individual units of larger apparent height that were  
195 scattered across the surface. The data showed no indication of  
196 Th-modified single-decker species.<sup>66</sup> Taking a height profile  
197 along the gray line revealed that the individual species  
198 embedded in the 2H-TPP monolayer and the compact  
199 Th(TPP)<sub>2</sub> island exhibited the same apparent height (see  
200 Figure 2d). Accordingly, the former were assigned to  
201 Th(TPP)<sub>2</sub> units. The coexistence of compact Th(TPP)<sub>2</sub> arrays  
202 and individual Th(TPP)<sub>2</sub> units was reminiscent to the  
203 situation of in situ synthesized Ce(TPP)<sub>2</sub><sup>58</sup> and Gd(Pc)<sub>2</sub><sup>59</sup>  
204 on Ag(111). Similar to other tetrapyrrole double-decker  
205 complexes,<sup>52,59</sup> the apparent height of Th(TPP)<sub>2</sub> was strongly  
206 bias-dependent because it reflected the electronic structure of  
207 the complex (see below). Accordingly, a meaningful  
208 comparison of apparent heights of chemically different  
209 M(TPP)<sub>2</sub> units was not straightforward. It is noted that the  
210 apparent height of M(TPP)<sub>2</sub> increased with increasing positive  
211 sample bias voltage until a height value was reached that stayed  
212 roughly constant with further moderate increase of the bias.  
213 When considering the apparent height at bias voltages where

214 this "plateau" was reached (1.9 V for Th(TPP)<sub>2</sub>, 2.4 V for  
215 Ce(TPP)<sub>2</sub>), the values for Th(TPP)<sub>2</sub> (0.34 nm) and  
216 Ce(TPP)<sub>2</sub> (0.33 nm)<sup>58</sup> measured relative to the surrounding  
217 2H-TPP layer compared well. Given the similar covalent<sup>84</sup> and  
218 ionic radii<sup>77</sup> of Th and Ce, this finding was not surprising.  
219 Because of their apparent height of 0.78 nm (with regard to  
220 2H-TPP), the additional bright species within the Th(TPP)<sub>2</sub>  
221 island were tentatively assigned to Th<sub>2</sub>(TPP)<sub>3</sub> triple-decker  
222 species.

223 The electronic properties of Th(TPP)<sub>2</sub>/Ag(111) were  
224 explored by STS. Figure 2f represents a typical dI/dV spectrum  
225 taken above the center of an individual Th(TPP)<sub>2</sub> double-  
226 decker (see black marker in Figure 2e), showing well-defined  
227 features. The unoccupied spectral region ( $V_b > 0$  V) was  
228 dominated by a distinct peak at 1290 mV trailed by a shoulder  
229 and a negative differential resistance (NDR) region. At  $\sim 670$   
230 mV a faint double protrusion was observed. Because its lower-  
231 energy peak (onset at  $\sim 540$  mV) was the first unoccupied  
232 feature detected, it was associated with the lowest unoccupied  
233 molecular orbital (LUMO). The occupied spectral region ( $V_b$   
234  $< 0$  V) revealed an onset at approximately  $-1950$  mV, which  
235 was tentatively assigned to the highest occupied molecular  
236 orbital (HOMO). Consequently, the apparent HOMO-  
237 LUMO gap amounted to  $\sim 2490$  mV. Within an experimental  
238 accuracy of  $\pm 30$  mV (i.e., given by the lateral and vertical  
239 positions of the tip), the spectra recorded on several Th(TPP)<sub>2</sub>  
240 units provided consistent values for the characteristic spectral  
241 features. While their assignment to distinct molecular orbitals  
242 was not straightforward, some conclusions could be drawn  
243 from the spectra. The low conductivity around the Fermi level  
244 ( $E_F$ ,  $V_b = 0$  V) and the corresponding emergence of an  
245 electronic gap, as well as the NDR signature, indicated a weak  
246 interaction of the probed molecular states with the metallic  
247 support. Reference spectra recorded on 2H-TPP (gray marker  
248 in Figure 2e) did not show a gap but rather broad resonances.  
249 Interestingly, the onset of the prominent feature in the  
250 unoccupied range that was previously assigned to the LUMO

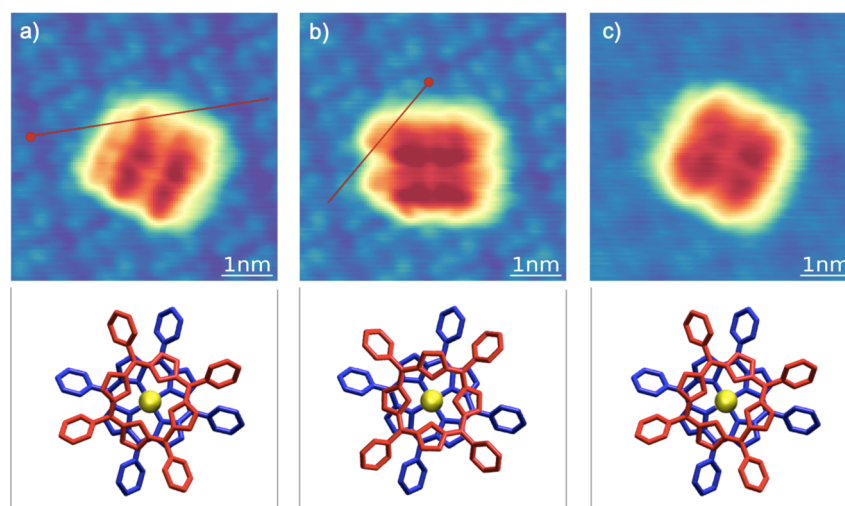


**Figure 4.** Reversible tip-induced mechanical rotation of the top porphyrin in individual  $\text{Th}(\text{TPP})_2$  units. (Top row) STM images of a double-decker embedded in a 2H-TPP array. (Bottom row) Corresponding structural models (top view). (a) Initial configuration. By laterally moving the tip from the position marked by the red dot along the red line, a rotation of the top porphyrin is induced. (b)  $\text{Th}(\text{TPP})_2$  after this first manipulation step. The red line marks the subsequently applied manipulation path. (c) In this second manipulation step, the  $\text{Th}(\text{TPP})_2$  returned to its initial configuration. The apparent change in resolution is related to a minor modification of the STM tip apex. Lateral manipulation parameters:  $I_t = 3.5$  nA,  $V_b = 0.05$  V. Scanning parameters:  $I_t = 0.11$  nA,  $V_b = 1.7$  V.

251 of 2H-TPP<sup>66,85</sup> coincided with the onset of the LUMO of  
252  $\text{Th}(\text{TPP})_2$ .

253 On a more general note, the overall spectral shape including  
254 the features described earlier for  $\text{Th}(\text{TPP})_2$  was reflected in  
255 several different bis(tetrapyrrole)lanthanoid systems on  
256  $\text{Ag}(111)$  and  $\text{Cu}(111)$ ,<sup>47,57</sup> even if the energies of the features  
257 depended on the specific center atom, the tetrapyrroles, and  
258 the substrate involved. Nonetheless, as far as we know, a  
259 conclusive interpretation of these features is lacking in the  
260 literature to date. The apparent HOMO–LUMO gap of  
261  $\text{Th}(\text{TPP})_2/\text{Ag}(111)$  exceeded the ones of  $\text{Ce}(\text{TPP})_2/\text{Ag}(111)$   
262 ( $\sim 2160$  mV)<sup>47</sup> and  $\text{CePcTPP}/\text{Ag}(111)$  ( $\sim 1550$  mV).<sup>57</sup>  
263 Whereas the latter case highlighted the influence of the Pc  
264 ligand in the heteroleptic complex, the two homoleptic TPP  
265 systems revealed the influence of the central atom.

266 In a next step, we aimed for a detailed insight into the self-  
267 assembled  $\text{Th}(\text{TPP})_2$  arrays and shed some light on the  
268 conformation of the double-deckers. Figure 3 a shows an STM  
269 image of a  $\text{Th}(\text{TPP})_2$  island embedded in a 2H-TPP array  
270 featuring intramolecular resolution. At a bias voltage of  $V_b =$   
271 2.0 V, the 2H-TPPs showed a square-like shape with four  
272 protrusions and a central depression, as previously reported.<sup>86</sup>  
273 The  $\text{Th}(\text{TPP})_2$ , on the other hand, featured a more rectangular  
274 shape with four extended protrusions, peripheral lobes, and a  
275 central depression. Because of the apparent 2-fold symmetry of  
276 the double-decker at this specific bias voltage, we defined a  
277 main symmetry axis along the dark central line crossing the  
278  $\text{Th}(\text{TPP})_2$  (see Figure 3a). A model overlay of the top  
279 porphyrin showed that this main axis represented the N–Th–  
280 N directions and indicated that the phenyl ring orientations as  
281 well as a nonplanar macrocycle distortion contributed to the 2-  
282 fold appearance. Importantly, two distinct orientations of the  
283 porphyrin top ligand of  $\text{Th}(\text{TPP})_2$  were observed, differing by  
284  $\sim 90^\circ$  (see dark and light-red rectangular outlines in Figure 3a).  
285 In the molecular array, the orientation alternated from  
286 molecule to molecule. The centers of  $\text{Th}(\text{TPP})_2$  were placed  
287 on positions in the registry with the surrounding 2H-TPP  
288 lattice with a nearest-neighbor distance of 1.39 nm (see blue

grid in Figure 3a), implying that the  $\text{Th}(\text{TPP})_2$ 's bottom 289  
ligands followed the packing of the 2H-TPPs. On the basis of 290  
this assumption, one could determine the twist angle  $\alpha$  291  
between the bottom and top macrocycles of  $\text{Th}(\text{TPP})_2$ , which 292  
amounted to  $(33 \pm 6)^\circ$  for the dark-red species. This value 293  
matched the twist angle of  $\sim 30^\circ$  reported for crystalline 294  
 $\text{Th}(\text{TPP})_2$  and indicated deviations from a square, anti- 295  
prismatic coordination geometry.<sup>37</sup> For the bright-red species, 296  
 $\alpha = (-56 \pm 6)^\circ$  (with “–” signaling counterclockwise 297  
rotation), reflecting the same macrocycle registry if a 4-fold 298  
symmetry of the macrocycle was assumed. Additionally, 299  
 $\text{Th}(\text{TPP})_2$  featuring the opposite chirality, i.e., twist angles of 300  
 $(-33 \pm 6)^\circ$  or  $(56 \pm 6)^\circ$ , occurred in islands with identical 301  
packing. The same twist angles were found for individual 302  
double-deckers embedded in 2H-TPP, which signaled that 303  
packing effects did not play a dominant role. The conformation 304  
of  $\text{Th}(\text{TPP})_2$  thus differed from that of  $\text{Ce}(\text{TPP})_2$ , where twist 305  
angles of  $(15 \pm 5)^\circ$  and  $(45 \pm 5)^\circ$  were reported for individual 306  
and dense-packed double-deckers, respectively.<sup>58</sup> Nonetheless, 307  
the packing scheme featuring alternating orientations of top 308  
ligands differing by  $90^\circ$  was reminiscent of self-assembled 309  
 $\text{Ce}(\text{TPP})_2$  islands on  $\text{Ag}(111)$ .<sup>58</sup> 310

A more detailed insight into the structure of  $\text{Th}(\text{TPP})_2$  311  
adsorbed on  $\text{Ag}(111)$  was provided by DFT (Figure 3b–d and 312  
Figure S1 in the Supporting Information). The calculations 313  
revealed that the top and bottom ligands displayed different 314  
geometries. The bottom porphyrin, coupled to the metallic 315  
substrate, exhibited a saddle conformation and a moderate tilt 316  
of the peripheral phenyl groups (dihedral angles  $\sim 40^\circ$ ). The 317  
top ligand adopted an inverted dome shape and a larger tilt of 318  
the phenyl rings (dihedral angles from  $64^\circ$  to  $86^\circ$ , average = 319  
 $74^\circ$ ). From the superposition of the STM image simulation 320  
and the double-decker structure (see Figure 3b), one could see 321  
that the STM contrast was entirely governed by the four 322  
phenyl rings of the top ligand. The quantitative agreement 323  
between STM simulations and experiments indeed allowed 324  
one to assign the dark central line (characteristic of the 325  
 $\text{Th}(\text{TPP})_2$  appearance at 2 V) to a N–Th–N axis, with the 2- 326

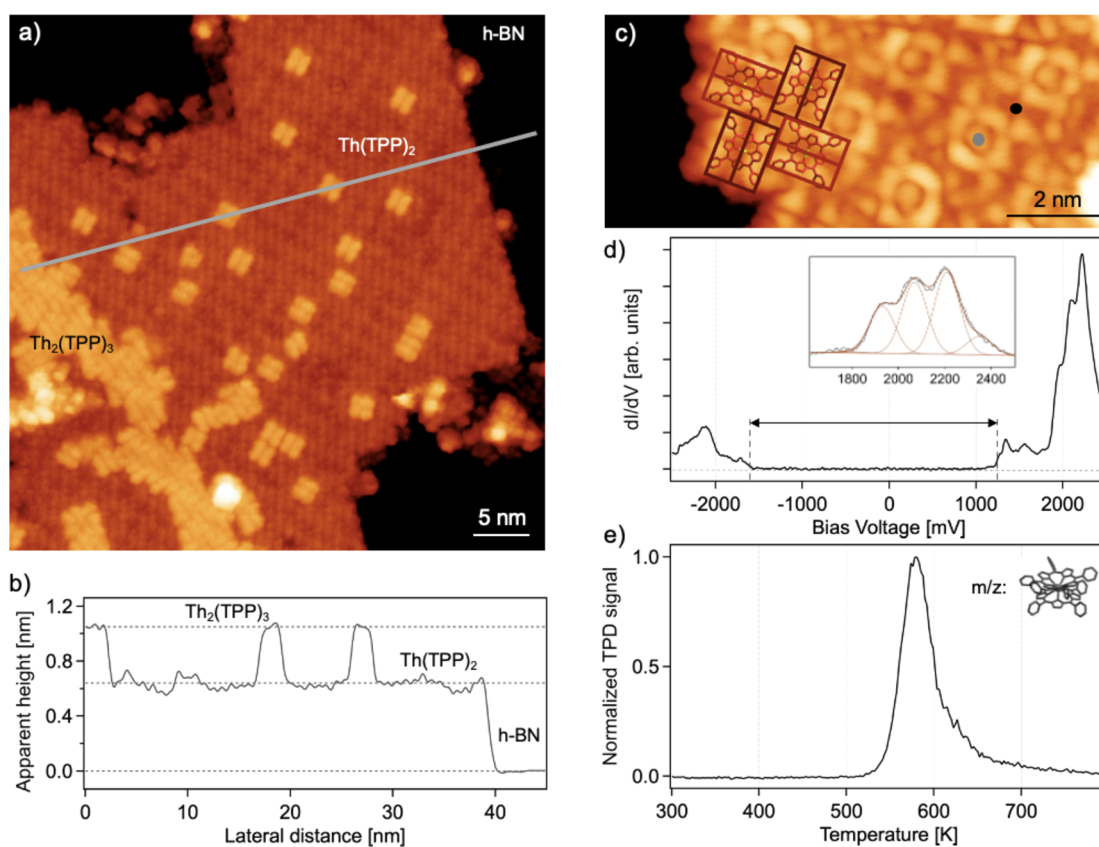


**Figure 5.** (a) STM image of a self-assembled  $\text{Th}(\text{TPP})_2$  island on  $h\text{-BN}/\text{Cu}(111)$ . Third-layer species within the island are tentatively attributed to  $\text{Th}_2(\text{TPP})_3$ . (b) Height profile along the line highlighted in panel a. (c) STM image of a  $\text{Th}(\text{TPP})_2$  island revealing the same packing as on  $\text{Ag}(111)$ . Two orientations of top porphyrins rotated by  $\sim 90^\circ$  with respect to each other are observed, as highlighted by the superimposed rectangles and models (compare to Figure 3a). (d)  $dI/dV$  spectrum of  $\text{Th}(\text{TPP})_2$  (averaged from three individual spectra) recorded above the center of the molecule (see black marker in panel c). The arrow marks the apparent gap. The inset shows a magnification of the substructure of the main peak (recorded above the position represented by the gray marker in panel c) after subtracting a polynomial background. The signal is fitted by four Gaussians with fixed separation and fixed width. Tip stabilized at  $I_t = 100$  pA,  $V_b = 2.0$  V,  $z\text{-approach} = 0.5$  Å. (e) TPD spectrum of the relevant mass-to-charge ratio  $m/z$ , showing the desorption of  $\text{Th}(\text{TPP})_2$  around 580 K. Scanning parameters: (a)  $I_t = 0.8$  nA,  $V_b = 1.725$  V; (c)  $I_t = 0.5$  nA,  $V_b = 2.0$  V.

327 fold symmetry induced by the phenyl groups tilted in opposite  
 328 directions (see Figure 3b–d). Interestingly, DFT yielded a  
 329 higher stability (by 60 meV) for a  $\text{Th}(\text{TPP})_2$  configuration  
 330 with a twist angle  $\alpha = 30^\circ$  than for the one with  $\alpha = 45^\circ$ , thus  
 331 confirming the experimental observation (which seems  
 332 counterintuitive when only considering steric repulsion).  
 333 Additional structural information (such as Th–N bond lengths  
 334 and  $\text{Th}(\text{TPP})_2$  adsorption heights) extracted from the DFT  
 335 optimization is provided in Figure S1, including a comparison  
 336 of  $\text{Th}(\text{TPP})_2$  on  $\text{Ag}(111)$ ,  $\text{Cu}(111)$ , and  $h\text{-BN}$ . It is noted that  
 337 the inverted dome shape observed for the top decker might  
 338 promote distinct interactions with nonplanar guest species,  
 339 such as fullerenes.<sup>47</sup>

340 Next, we experimentally addressed the structural stability of  
 341  $\text{Th}(\text{TPP})_2$  and demonstrated the rotatability of the upper  
 342 porphyrin by applying an STM-based molecular manipulation  
 343 procedure. First, an STM image with scanning parameters not  
 344 affecting the  $\text{Th}(\text{TPP})_2$  was taken. Then, the STM tip  
 345 approached the surface and laterally moved across the  
 346 periphery of the upper porphyrin of the double-decker to  
 347 exert a torque, keeping the current constant. Subsequently, the  
 348 tip was retracted, and another STM image with the original  
 349 parameters was taken to check whether the manipulation was  
 350 successful. Figure 4 shows the reversible azimuthal rotation of

the top ligand of a  $\text{Th}(\text{TPP})_2$  anchored in the 2H-TPP 351  
 network by applying said procedure. Starting from the position 352  
 marked by a red dot, the STM tip was moved along the red 353  
 path, rotating the upper TPP out of its equilibrium orientation. 354  
 From the initial configuration in Figure 4a, an apparent 355  
 clockwise rotation of  $\sim 70^\circ$  led to the configuration in Figure 356  
 4b. Using the same manipulation procedure but a different tip 357  
 path, the process could be reversed, as shown by the apparent 358  
 counterclockwise rotation from panel b to panel c of Figure 4, 359  
 after which the molecule was again in its initial state. During 360  
 the whole procedure, the top porphyrin remained in registry 361  
 with the unaffected 2H-TPP network. The two distinct 362  
 configurations (Figure 4a and b) reflected the twist angles as 363  
 discussed earlier. These lateral manipulation experiments were 364  
 performed successfully on several molecules. In some cases, the 365  
 removal of the complete  $\text{Th}(\text{TPP})_2$  occurred, exposing a bare 366  
 $\text{Ag}(111)$  patch.<sup>52</sup> Apparently, the interaction between the Th 367  
 center and the upper porphyrin macrocycle was sufficiently 368  
 strong to prevent decomposition of  $\text{Th}(\text{TPP})_2$  upon 369  
 interaction with the STM tip under the applied manipulation 370  
 parameters. This experiment also showed that the vertical 371  
 separation of the two TPP units by the Th center was large 372  
 enough to allow reversible rotational switching of the upper 373  
 porphyrin, even though details of the process (such as the 374

sense of rotation) remained elusive to the STM methodology. Nonetheless, STM measurements of this system carried out at room temperature showed a rectangular outline of the individual molecules as in the low-temperature imaging (not shown), indicating that the rotation barrier was high enough to inhibit thermally induced rotation on the time scale of the STM imaging, even at room temperature. Indeed, a DFT-calculated energy profile between two configurations revealed a considerable energy barrier with a transition state featuring aligned phenyl moieties of upper and lower porphyrin ligands (see Figure S2). In summary, we concluded that surface-anchored Th(TPP)<sub>2</sub> represented a molecular rotor switchable by an external stimulus, in agreement with findings for surface-confined lanthanide tetrapyrrole sandwich compounds.<sup>58,87,88</sup>

**Thorium Bis(porphyrinato) Complexes on *h*-BN/Cu(111).** After demonstrating the successful assembly of Th(TPP)<sub>2</sub> double-decker complexes on the Ag(111) surface, we now discuss the results of applying the same synthesis protocol to the *h*-BN/Cu(111) support (see Figure 1e), again yielding the targeted Th(TPP)<sub>2</sub> complexes. The *h*-BN spacer layer was introduced to access intrinsic molecular properties, reducing potentially detrimental effects on electronic and magnetic characteristics caused by interaction with a metallic support.<sup>50,51,55</sup> Figure 5a shows an STM image of the resulting surface structure. Dense-packed islands of Th(TPP)<sub>2</sub> embedding individual, as well as aggregated, third-layer molecules were observed. However, no surrounding 2H-TPP layer remained on the surface. This allowed for determination of the apparent height of the complexes relative to the bare *h*-BN support. The line profile in Figure 5b reveals an apparent height of 0.64 nm (at  $V_b = 1.725$  V) for the island assigned to Th(TPP)<sub>2</sub> and of 1.05 nm for the third-layer species.

Submolecularly resolved STM images exhibited the same order of the Th(TPP)<sub>2</sub> islands as on Ag(111) (Figure 5c). Specifically, a 2-fold appearance of Th(TPP)<sub>2</sub> was observed at  $V_b = 2$  V, and every second upper TPP ligand was rotated by  $\sim 90^\circ$  with respect to its neighbors, as reflected by the framed dark- and light-red models superimposed on the STM image in Figure 5c. Because no 2H-TPP was left as a “marker” for the orientation of the bottom TPP, the twist angle of Th(TPP)<sub>2</sub>/*h*-BN/Cu(111) remained elusive in our experiment. DFT modeling (Figure S1) revealed a similar conformation for Th(TPP)<sub>2</sub> on Ag(111) and *h*-BN, with a larger adsorption height on the latter support.

The absence of 2H-TPP after annealing the Th-exposed 2H-TPP multilayer at 500 K showed that unreacted 2H-TPP readily desorbed from *h*-BN/Cu(111) at this temperature, whereas Th(TPP)<sub>2</sub> only efficiently desorbed at higher temperature (see below). Indeed, the desorption of a somewhat smaller tetrapyrrole (2H-porphine) from *h*-BN/Cu(111) occurred at 470 K.<sup>89</sup>

A characteristic STS signature of a Th(TPP)<sub>2</sub> complex on *h*-BN/Cu(111) is shown in Figure 5d. Even though the key features already discussed for the  $dI/dV$  spectrum of Th(TPP)<sub>2</sub>/Ag(111) remained clearly discernible, the spectrum on Th(TPP)<sub>2</sub>/*h*-BN showed distinct modifications. The dominant resonance in the unoccupied spectral region appeared at  $\sim 2000$  mV and showed a pronounced substructure with a series of peaks separated by an average spacing of  $(142 \pm 5)$  mV (see inset in Figure 5d). A faint feature with an onset at  $\sim 1240$  mV was assigned to the LUMO, following the notation introduced earlier for Th(TPP)<sub>2</sub>/Ag(111). The occupied spectral feature comprised a subtle increase in

conductivity at approximately  $-1650$  mV, the HOMO, which followed by a peak at  $-2130$  mV. Accordingly, the apparent HOMO–LUMO gap (2890 mV) of Th(TPP)<sub>2</sub>/*h*-BN/Cu(111) was noticeably increased by  $\sim 400$  mV compared to Th(TPP)<sub>2</sub> adsorbed on Ag(111), pointing to an efficient electronic decoupling of Th(TPP)<sub>2</sub> from the Cu(111) by the *h*-BN spacer. Indeed, the substructure of the main resonance was reminiscent of vibronic excitations, as reported for phthalocyanines on *h*-BN/Ir(111) and *h*-BN/Rh(111).<sup>90,91</sup> However, both the intensity sequence and the peak separation were distinct. The measured energy spacing (142 mV,  $1145 \text{ cm}^{-1}$ ) and the rescaled energy spacing, considering the voltage drop across the *h*-BN layer<sup>91</sup> ( $118 \text{ mV}$ ,  $952 \text{ cm}^{-1}$ ), fell in a range of different vibrational modes reported for Th(TPP)<sub>2</sub>.<sup>38</sup> It should be noted that the energy of Th(TPP)<sub>2</sub>'s spectral features could vary with lateral position due to the corrugated electronic landscape provided by the *h*-BN/Cu(111) support.<sup>92</sup>

To corroborate the in situ formation of Th(TPP)<sub>2</sub> complexes and to study the corresponding desorption characteristics, a qualitative TPD characterization was carried out. A Th(TPP)<sub>2</sub>/*h*-BN/Cu(111) sample was prepared by the procedure described earlier and subsequently annealed with a linear heating rate (1 K/s), recording the signal that corresponded to the mass-to-charge ratio of the thorium porphyrinato double-decker (1456 amu). Specifically, due to the limited resolution at such a high mass, we integrated over a small mass range ( $1456 \pm 10$  amu). A typical desorption spectrum is depicted in Figure 5e, revealing a maximum at a temperature of  $\sim 580$  K. The TPD experiment thus provided two important messages. (1) The detection of the Th(TPP)<sub>2</sub> proved the successful in situ synthesis of bis(porphyrinato) thorium on *h*-BN/Cu(111), complementing the STM data. (2) The *h*-BN support afforded the thermal desorption of intact, interfacial tetrapyrrole adsorbates and reaction products that could subsequently be characterized, e.g., by mass spectrometry, complementing TPD results on porphyrin multilayers and films.<sup>63,64</sup>

## CONCLUSIONS

We introduced actinides for interfacial coordination chemistry. Specifically, we reported the fabrication of homoleptic thorium bis(porphyrinato) complexes, namely, Th(TPP)<sub>2</sub>, on well-defined model surfaces under UHV conditions. The N 1s and Th 4f XPS data revealed the bonding of the Th center to the TPP macrocycles. Submolecular resolution in STM imaging combined with complementary DFT modeling gave insight into the conformation of Th(TPP)<sub>2</sub>, characterized by distinct twist angles between bottom and top porphyrin ligands ( $33^\circ$  and  $56^\circ$ ), an inverted dome shape of the latter, and tilted terminal phenyl moieties. The twist angles deviated from the ones reported for its lanthanide counterpart, Ce(TPP)<sub>2</sub> on Ag(111), reflecting the character of the actinide center. The self-assembled Th(TPP)<sub>2</sub> arrays on Ag(111) and *h*-BN/Cu(111) showed the same packing, with alternating orientations of the top ligands differing by  $90^\circ$ , consistent with reports on the Ce(TPP)<sub>2</sub> islands. The reversible rotation of the top porphyrin by tip manipulation demonstrated the potential of actinide-based tetrapyrrole double-deckers for molecular switching and machinery, with the large size of the Th ion facilitating rotational dynamics by separation of the two macrocycles. From a different perspective, this study showed for the first time the formation of a supramolecular double-

500 decker complex on a two-dimensional material, namely,  
501 monolayer *h*-BN, and demonstrated the benefits of such a  
502 decoupling layer. Specifically, the *h*-BN support permitted the  
503 thermal desorption of intact double-decker units, corroborat-  
504 ing the successful in situ Th(TPP)<sub>2</sub> synthesis, and allowed one  
505 to observe details of the double-deckers's electronic structure  
506 including vibronic signatures by STS. Thus, no metal surface  
507 was needed as a catalyst for this multistep synthesis of actinide-  
508 based metal–organic complexes.

509 We anticipate that the reported synthesis protocol is  
510 generally applicable to diverse tetrapyrrole derivatives, addi-  
511 tional actinide elements, and other supports (including two-  
512 dimensional materials), thus opening pathways to actinide  
513 complexes and nanostructures with tailored properties and  
514 functionalities. Accordingly, surface-confined actinide-based  
515 metal–organic complexes and supramolecular architectures  
516 might perfectly complement lanthanide-based systems for  
517 potential application in molecular magnetism, quantum  
518 technologies, sensing, and heterogeneous catalysis.

## 519 ■ EXPERIMENTAL SECTION

520 **Experimental Setup and Data Processing.** XPS measurements  
521 were conducted in a custom-built UHV chamber incorporating a XPS  
522 system with a lab-based X-ray source and a hemispherical electron  
523 analyzer from SPECS (Phoibos 100). All data were acquired using a  
524 Mg anode (1253.6 eV) with a pass energy of 10 eV in normal  
525 emission. During the acquisition of the XP spectra, the base pressure  
526 was  $<1 \times 10^{-9}$  mbar and the sample was kept at rt. The spectra were  
527 calibrated against the binding energy of the Ag 3d<sub>5/2</sub> core level.  
528 Pseudo-Voigt functions were used to fit the spectra. The background  
529 in the Th 4f spectra was corrected by subtracting a Shirley  
530 background following the method of Herrera-Gomez et al.<sup>93</sup> For  
531 the N 1s spectra, the background subtraction was performed by fitting  
532 the clean Ag(111) signal with a polynomial function and subtracting  
533 this adjusted curve from the data.

534 STM measurements were carried out in a separate custom-built  
535 UHV system housing a commercial low-temperature CreaTec STM  
536 operating at 7 K with a base pressure of  $<3 \times 10^{-10}$  mbar. All images  
537 were recorded in constant-current mode using a chemically etched W  
538 tip.

539 The TPD experiments were performed in a custom-designed UHV  
540 chamber with a base pressure of low  $10^{-10}$  mbar, which could be  
541 lowered to  $6 \times 10^{-11}$  mbar during the TPD acquisition by employing  
542 liquid nitrogen cooled traps. A K-type junction, which was in direct  
543 contact with the Cu(111) crystal, was used to measure the  
544 temperature of the sample. The quadrupole mass spectrometer  
545 (QMS) used in the TPD experiments was a Balzers QMA 160 rod  
546 system enclosed within a copper cap,<sup>94</sup> in front of which the Cu(111)  
547 crystal was positioned as close as 1 mm. A mass range up to 3000 amu  
548 was covered with 400 kHz Extrel electronics. The temperature was  
549 varied linearly, exploiting radiative heating from a glowing W filament  
550 placed behind the sample and using a purpose-built PID controller  
551 (Schlichting Physikalische Instrumente HS 130). The experimental  
552 chamber also contained XPS equipment (a dual-anode X-ray source  
553 and a SPECS Phoibos 100 hemispherical electron analyzer with 2D-  
554 CCD detector) for optimization of the preparation procedures and  
555 consistency checks. STM data were processed using Gwyddion,<sup>95</sup>  
556 python3, and the WSxM software ([www.wsxm.es](http://www.wsxm.es)). A Gaussian filter  
557 was applied to Figure 3a.

558 **Sample Preparation.** The Ag(111) and Cu(111) single crystals  
559 were cleaned by repeated cycles of Ar<sup>+</sup> or Ne<sup>+</sup> sputtering at an energy  
560 of 800–1000 eV and annealing to  $\sim 730$  K (silver) and  $\sim 830$  K  
561 (copper) for several minutes. The 2H-TPP molecules (Sigma-Aldrich,  
562  $\geq 99\%$  purity) were evaporated via organic molecular beam epitaxy  
563 (OMBE) from a quartz crucible that was resistively heated to  $T_{\text{evap}} \approx$   
564 260 °C, while the sample was kept at rt. Th atoms were deposited  
565 from a home-built water-cooled evaporator with integrated temper-

ature-stabilized quartz microbalance. Our source was a 0.2 mm Th 566  
wire (Goodfellow, 99.5% purity) wrapped by multiple windings (0.5 567  
mm pitch) of a 0.1 mm W wire onto a 0.3 mm W support wire. The 568  
whole assembly was resistively heated, and the evaporation rate was 569  
measured with the microbalance; see ref 96 for details. The *h*-BN 570  
monolayer was grown by chemical vapor deposition of borazine 571  
(B<sub>3</sub>N<sub>3</sub>H<sub>6</sub>, Katchem, Czech Republic), following a published recipe.<sup>75</sup> 572

**Theoretical Methodology.** DFT calculations were carried out 573  
using the Vienna Ab Initio Simulation Package (VASP)<sup>97</sup> with the 574  
Perdew–Burke–Ernzerhof (PBE) exchange correlation.<sup>98</sup> The 575  
projector-augmented wave potential with a cutoff energy of 400 eV 576  
was used to describe the electron–ion interaction.<sup>99</sup> We considered 577  
the metallic lattice parameter  $a_{\text{Ag}} = 4.07$  Å (corresponding to a Ag– 578  
Ag distance of 2.878 Å). Hence, we used the GGA PBE-D3 579  
method<sup>100</sup> to achieve structural and electronic convergence of the 580  
large supercells at Gamma point. The simulated STM images were 581  
carried out by applying the Tersoff and Hamann theory in a plane- 582  
wave basis set as implemented in the STMpw code.<sup>101</sup> To visualize 583  
the simulations, we used Crystal Maker 10 software ([www. 584](http://www.crystallmaker.com)  
[crystallmaker.com](http://www.crystallmaker.com)).

## ■ ASSOCIATED CONTENT

### Supporting Information

The Supporting Information is available free of charge at 588  
<https://pubs.acs.org/doi/10.1021/jacs.1c04982>. 589

Additional structural information from DFT calcula- 590  
tions, including coordinates of Th(TPP)<sub>2</sub> (PDF) 591

## ■ AUTHOR INFORMATION

### Corresponding Author

Willi Auwärter – Physics Department E20, Technical 594  
University of Munich, D-85748 Garching, Germany; 595  
[orcid.org/0000-0001-9452-4662](https://orcid.org/0000-0001-9452-4662); Email: [wau@tum.de](mailto:wau@tum.de) 596

### Authors

Erik Rheinfrank – Physics Department E20, Technical 597  
University of Munich, D-85748 Garching, Germany 598  
Mathias Pörtner – Physics Department E20, Technical 600  
University of Munich, D-85748 Garching, Germany 601  
Maria del Carmen Nuñez Beyerle – Physics Department 602  
E20, Technical University of Munich, D-85748 Garching, 603  
Germany 604  
Felix Haag – Physics Department E20, Technical University of 605  
Munich, D-85748 Garching, Germany 606  
Peter S. Deimel – Physics Department E20, Technical 607  
University of Munich, D-85748 Garching, Germany 608  
Francesco Allegretti – Physics Department E20, Technical 609  
University of Munich, D-85748 Garching, Germany; 610  
[orcid.org/0000-0001-6141-7166](https://orcid.org/0000-0001-6141-7166) 611  
Knud Seufert – Physics Department E20, Technical University 612  
of Munich, D-85748 Garching, Germany; [orcid.org/ 613](https://orcid.org/0000-0002-4111-0965)  
[0000-0002-4111-0965](https://orcid.org/0000-0002-4111-0965) 614  
Johannes V. Barth – Physics Department E20, Technical 615  
University of Munich, D-85748 Garching, Germany; 616  
[orcid.org/0000-0002-6270-2150](https://orcid.org/0000-0002-6270-2150) 617  
Marie-Laure Bocquet – PASTEUR, Département de Chimie, 618  
Ecole Normale Supérieure, PSL University, Sorbonne 619  
Université, CNRS, F-75005 Paris, France; [orcid.org/ 620](https://orcid.org/0000-0001-7122-4907)  
[0000-0001-7122-4907](https://orcid.org/0000-0001-7122-4907) 621  
Peter Feulner – Physics Department E20, Technical 622  
University of Munich, D-85748 Garching, Germany 623

Complete contact information is available at: 624  
<https://pubs.acs.org/doi/10.1021/jacs.1c04982> 625

## 626 Notes

627 The authors declare no competing financial interest.

## 628 ■ ACKNOWLEDGMENTS

629 We thank Nicolas Lorente for fruitful discussions. This work  
630 was supported by the European Research Council Consol-  
631 idator Grant NanoSurfs (no. 615233), the ANR-DFG project  
632 RidePorph, and the Deutsche Forschungsgemeinschaft (DFG)  
633 via the Cluster of Excellence e-conversion. M.-L.B. acknowl-  
634 edges granted access to the French HPC resources of TGCC  
635 and CINES under Grant A7-A0070807364 by GENCI. F.H.,  
636 F.A., and J.V.B. are grateful for funding from the TUM  
637 International Graduate School of Science and Engineering  
638 (IGSSE) via the DFG, GSC 81. W.A. acknowledges funding by  
639 the DFG via a Heisenberg professorship.

## 640 ■ REFERENCES

- 641 (1) Arnold, P. L.; Casely, I. J. F-Block N-Heterocyclic Carbene  
642 Complexes. *Chem. Rev.* **2009**, *109*, 3599–3611.
- 643 (2) Albrecht-Schmitt, T. E. Actinide Materials Adopt Curvature:  
644 Nanotubules and Nanospheres. *Angew. Chem., Int. Ed.* **2005**, *44*,  
645 4836–4838.
- 646 (3) Jones, M. B.; Gaunt, A. J. Recent Developments in Synthesis and  
647 Structural Chemistry of Nonaqueous Actinide Complexes. *Chem. Rev.*  
648 **2013**, *113*, 1137–1198.
- 649 (4) Edelmann, F. T.; Farnaby, J. H.; Jaroschik, F.; Wilson, B.  
650 Lanthanides and actinides: Annual survey of their organometallic  
651 chemistry covering the year 2018. *Coord. Chem. Rev.* **2019**, *398*,  
652 113005.
- 653 (5) Neidig, M. L.; Clark, D. L.; Martin, R. L. Covalency in f-element  
654 complexes. *Coord. Chem. Rev.* **2013**, *257*, 394–406.
- 655 (6) Ward, A. L.; Buckley, H. L.; Lukens, W. W.; Arnold, J. Synthesis  
656 and Characterization of Thorium(IV) and Uranium(IV) Corrole  
657 Complexes. *J. Am. Chem. Soc.* **2013**, *135*, 13965–13971.
- 658 (7) Klamm, B. E.; Windorff, C. J.; Celis-Barros, C.; Marsh, M. L.;  
659 Meeker, D. S.; Albrecht-Schmitt, T. E. Experimental and Theoretical  
660 Comparison of Transition-Metal and Actinide Tetravalent Schiff Base  
661 Coordination Complexes. *Inorg. Chem.* **2018**, *57*, 15389–15398.
- 662 (8) Walter, O. Actinide Organometallic Complexes with  $\pi$ -Ligands.  
663 *Chem. - Eur. J.* **2019**, *25*, 2927–2934.
- 664 (9) Moore, K. T.; van der Laan, G. Nature of the *Sf* states in actinide  
665 metals. *Rev. Mod. Phys.* **2009**, *81*, 235–298.
- 666 (10) Gibson, J. K. Gas-phase chemistry of actinide ions: probing the  
667 distinctive character of the *Sf* elements. *Int. J. Mass Spectrom.* **2002**,  
668 *214*, 1–21.
- 669 (11) Cheisson, T.; Kersey, K. D.; Mahieu, N.; McSkimming, A.;  
670 Gau, M. R.; Carroll, P. J.; Schelter, E. J. Multiple Bonding in  
671 Lanthanides and Actinides: Direct Comparison of Covalency in  
672 Thorium(IV)- and Cerium(IV)-Imido Complexes. *J. Am. Chem. Soc.*  
673 **2019**, *141*, 9185–9190.
- 674 (12) Berryman, V. E. J.; Whalley, Z. J.; Shephard, J. J.; Ochiai, T.;  
675 Price, A. N.; Arnold, P. L.; Parsons, S.; Kaltsoyannis, N. Computa-  
676 tional analysis of M-O covalency in  $M(\text{OC}_6\text{H}_5)_4$  ( $M = \text{Ti}, \text{Zr}, \text{Hf},$   
677  $\text{Ce}, \text{Th}, \text{U}$ ). *Dalton Trans.* **2019**, *48*, 2939–2947.
- 678 (13) Rinehart, J. D.; Harris, T. D.; Kozimor, S. A.; Bartlett, B. M.;  
679 Long, J. R. Magnetic Exchange Coupling in Actinide-Containing  
680 Molecules. *Inorg. Chem.* **2009**, *48*, 3382–3395.
- 681 (14) Rinehart, J. D.; Long, J. R. Exploiting single-ion anisotropy in  
682 the design of f-element single-molecule magnets. *Chem. Sci.* **2011**, *2*,  
683 2078–2085.
- 684 (15) Layfield, R. A. Organometallic Single-Molecule Magnets.  
685 *Organometallics* **2014**, *33*, 1084–1099.
- 686 (16) Ok, K. M.; Sung, J.; Hu, G.; Jacobs, R. M. J.; O'Hare, D. TOF-  
687 2: A Large 1D Channel Thorium Organic Framework. *J. Am. Chem.*  
688 *Soc.* **2008**, *130*, 3762–3763.
- 689 (17) Li, Y.; Weng, Z.; Wang, Y.; Chen, L.; Sheng, D.; Diwu, J.; Chai,  
690 Z.; Albrecht-Schmitt, T. E.; Wang, S. Surprising coordination for low-

- 691 valent actinides resembling uranyl(vi) in thorium(iv) organic hybrid  
692 layered and framework structures based on a graphene-like (6,3) sheet  
693 topology. *Dalton Trans.* **2016**, *45*, 918–921.
- (18) Dolgoplova, E. A.; Rice, A. M.; Shustova, N. B. Actinide-based  
694 MOFs: a middle ground in solution and solid-state structural motifs.  
695 *Chem. Commun.* **2018**, *54*, 6472–6483.
- (19) Dolgoplova, E. A.; Ejegebawo, O. A.; Martin, C. R.; Smith, M.  
697 D.; Setyawan, W.; Karakalos, S. G.; Henager, C. H.; zur Loye, H.-C.;  
698 Shustova, N. B. Multifaceted Modularity: A Key for Stepwise Building  
699 of Hierarchical Complexity in Actinide Metal-Organic Frameworks. *J.*  
700 *Am. Chem. Soc.* **2017**, *139*, 16852–16861.
- (20) Arnold, P. L.; Ochiai, T.; Lam, F. Y. T.; Kelly, R. P.; Seymour,  
702 M. L.; Maron, L. Metallacyclic actinide catalysts for dinitrogen  
703 conversion to ammonia and secondary amines. *Nat. Chem.* **2020**, *12*,  
704 654–659.
- (21) Andrea, T.; Eisen, M. S. Recent advances in organothorium and  
706 organouranium catalysis. *Chem. Soc. Rev.* **2008**, *37*, 550–567.
- (22) Fox, A. R.; Bart, S. C.; Meyer, K.; Cummins, C. C. Towards  
708 uranium catalysts. *Nature* **2008**, *455*, 341–349.
- (23) Ephritikhine, M. The vitality of uranium molecular chemistry at  
710 the dawn of the XXIst century. *Dalton Trans.* **2006**, 2501–2516.
- (24) Jantunen, K. C.; Scott, B. L.; Kiplinger, J. L. A comparative  
712 study of the reactivity of Zr(IV), Hf(IV) and Th(IV) metallocene  
713 complexes: Thorium is not a Group IV metal after all. *J. Alloys Compd.*  
714 **2007**, *444–445*, 363–368.
- (25) Girolami, G. S.; Milam, S. N.; Suslick, K. S. Synthesis and  
716 characterization of actinide mono and bis porphyrin complexes. *Inorg.*  
717 *Chem.* **1987**, *26*, 343–344.
- (26) Sessler, J. L.; Seidel, D.; Vivian, A. E.; Lynch, V.; Scott, B. L.;  
719 Keogh, D. W. Hexaphyrin(1.0.1.0.0.0): An Expanded Porphyrin  
720 Ligand for the Actinide Cations Uranyl (UO<sub>2</sub><sup>2+</sup>) and Neptunyl  
721 (NpO<sub>2</sub><sup>+</sup>). *Angew. Chem., Int. Ed.* **2001**, *40*, 591–594.
- (27) Sessler, J. L.; Gorden, A. E.; Seidel, D.; Hannah, S.; Lynch, V.;  
723 Gordon, P. L.; Donohoe, R. J.; Tait, C. D.; Keogh, D. W.  
724 Characterization of the interactions between neptunyl and plutonyl  
725 cations and expanded porphyrins. *Inorg. Chim. Acta* **2002**, *341*, 54–  
726 70.
- (28) Krivovichev, S. V.; Kahlenberg, V.; Kaindl, R.; Mersdorf, E.;  
728 Tananaev, I. G.; Myasoedov, B. F. Nanoscale Tubules in Uranyl  
729 Selenates. *Angew. Chem., Int. Ed.* **2005**, *44*, 1134–1136.
- (29) Tutson, C. D.; Gorden, A. E. Thorium coordination: A  
731 comprehensive review based on coordination number. *Coord. Chem.*  
732 *Rev.* **2017**, *333*, 27–43.
- (30) Wang, Y.; Liu, W.; Bai, Z.; Zheng, T.; Silver, M. A.; Li, Y.;  
734 Wang, Y.; Wang, X.; Diwu, J.; Chai, Z.; Wang, S. Employing an  
735 Unsaturated Th<sup>4+</sup> Site in a Porous Thorium-Organic Framework for  
736 Kr/Xe Uptake and Separation. *Angew. Chem., Int. Ed.* **2018**, *57*,  
737 5783–5787.
- (31) Li, P.; Wang, X.; Otake, K.-i.; Lyu, J.; Hanna, S. L.; Islamoglu,  
739 T.; Farha, O. K. Synthetic Control of Thorium Polyoxo-Clusters in  
740 Metal-Organic Frameworks toward New Thorium-Based Materials.  
741 *ACS Appl. Nano Mater.* **2019**, *2*, 2260–2265.
- (32) Bell, N. L.; Maron, L.; Arnold, P. L. Thorium Mono- and  
743 Bis(imido) Complexes Made by Reprotonation of cyclo-Metalated  
744 Amides. *J. Am. Chem. Soc.* **2015**, *137*, 10492–10495.
- (33) Lux, F.; Dempf, D.; Graw, D. Diphthalocyaninato-thorium(IV)  
746 and -uranium(IV). *Angew. Chem., Int. Ed. Engl.* **1968**, *7*, 819–820.
- (34) Martarano, L. A.; Wong, C.-P.; Horrocks, W. D.; Ponte-  
748 Goncalves, A. M. Luminescence of yttrium(III), lutetium(III), and  
749 thorium(IV) porphyrin complexes. *J. Phys. Chem.* **1976**, *80*, 2389–  
750 2393.
- (35) Dormond, A.; Belkalem, B.; Charpin, P.; Lance, M.; Vigner, D.;  
752 Folcher, G.; Guillard, R. Thorium and uranium porphyrins. Synthesis  
753 and crystal structure of bis(acetylacetonato)(2,3,7,8,12,13,17,18-  
754 octaethylporphyrinato)thorium(IV). *Inorg. Chem.* **1986**, *25*, 4785–  
755 4790.
- (36) Kadish, K. M.; Moninot, G.; Hu, Y.; Dubois, D.; Ibnlfassi, A.;  
757 Barbe, J. M.; Guillard, R. Double-decker actinide porphyrins and  
758 phthalocyanines. Synthesis and spectroscopic characterization of 759

- 760 neutral, oxidized, and reduced homo- and heteroleptic complexes. *J.*  
761 *Am. Chem. Soc.* **1993**, *115*, 8153–8166.
- 762 (37) Girolami, G. S.; Gorlin, P. A.; Milam, S. N.; Suslick, K. S.;  
763 Wilson, S. R. Bis(porphyrin)actinide complexes and their radical  
764 cations and dications. *J. Coord. Chem.* **1994**, *32*, 173–212.
- 765 (38) Lomova, T. N.; Berezin, B. D. Porphyrin Complexes with p, d,  
766 and fMetals in High Oxidation States: Structures, Electronic  
767 Absorption, and IR Spectra. *Russ. J. Coord. Chem.* **2001**, *27*, 85–104.
- 768 (39) Barth, J. V.; Costantini, G.; Kern, K. Engineering atomic and  
769 molecular nanostructures at surfaces. *Nature* **2005**, *437*, 671–679.
- 770 (40) Bonifazi, D.; Mohnani, S.; Llanes-Pallas, A. Supramolecular  
771 Chemistry at Interfaces: Molecular Recognition on Nanopatterned  
772 Porous. *Chem. - Eur. J.* **2009**, *15*, 7004–7025.
- 773 (41) Goronzy, D. P.; Ebrahimi, M.; Rosei, F.; Arramel, Fang, Y.; De  
774 Feyter, S.; Tait, S. L.; Wang, C.; Beton, P. H.; Wee, A. T. S.; Weiss, P.  
775 S.; Perepichka, D. F. Supramolecular Assemblies on Surfaces:  
776 patterning, Functionality, and Reactivity. *ACS Nano* **2018**, *12*,  
777 7445–7481.
- 778 (42) Grill, L.; Hecht, S. Covalent on-surface polymerization. *Nat.*  
779 *Chem.* **2020**, *12*, 115–130.
- 780 (43) Kumar, A.; Banerjee, K.; Liljeroth, P. Molecular assembly on  
781 two-dimensional materials. *Nanotechnology* **2017**, *28*, 082001.
- 782 (44) Auwärter, W. Hexagonal boron nitride monolayers on metal  
783 supports: Versatile templates for atoms, molecules and nanostruc-  
784 tures. *Surf. Sci. Rep.* **2019**, *74*, 1–95.
- 785 (45) Ecija, D.; Urgel, J. I.; Seitsonen, A. P.; Auwärter, W.; Barth, J. V.  
786 Lanthanide-Directed Assembly of Interfacial Coordination Architec-  
787 tures-From Complex Networks to Functional Nanosystems. *Acc.*  
788 *Chem. Res.* **2018**, *51*, 365–375.
- 789 (46) Katoh, K.; Yoshida, Y.; Yamashita, M.; Miyasaka, H.; Breedlove,  
790 B. K.; Kajiwara, T.; Takaishi, S.; Ishikawa, N.; Isshiki, H.; Zhang, Y. F.;  
791 Komeda, T.; Yamagishi, M.; Takeya, J. Direct Observation of  
792 Lanthanide(III)-Phthalocyanine Molecules on Au(111) by Using  
793 Scanning Tunneling Microscopy and Scanning Tunneling Spectros-  
794 copy and Thin-Film Field-Effect Transistor Properties of Tb(III)- and  
795 Dy(III)-Phthalocyanine Molecules. *J. Am. Chem. Soc.* **2009**, *131*,  
796 9967–9976.
- 797 (47) Vijayaraghavan, S.; Ecija, D.; Auwärter, W.; Joshi, S.; Seufert,  
798 K.; Seitsonen, A. P.; Tashiro, K.; Barth, J. V. Selective Supramolecular  
799 Fullerene-Porphyrin Interactions and Switching in Surface-Confined  
800 C60-Ce(TPP)2 Dyads. *Nano Lett.* **2012**, *12*, 4077–4083.
- 801 (48) Fahrenndorf, S.; Atodiresi, N.; Besson, C.; Caciuc, V.; Matthes,  
802 F.; Blügel, S.; Kögerler, P.; Bürgler, D. E.; Schneider, C. M. Accessing  
803 4f-states in single-molecule spintronics. *Nat. Commun.* **2013**, *4*, 2425.
- 804 (49) Cirera, B.; Matarrubia, J.; Kaposi, T.; Giménez-Agulló, N.;  
805 Paszkiewicz, M.; Klappenberger, F.; Otero, R.; Gallego, J. M.;  
806 Ballester, P.; Barth, J. V.; Miranda, R.; Galán-Mascarós, J. R.;  
807 Auwärter, W.; Ecija, D. Preservation of electronic properties of  
808 double-decker complexes on metallic supports. *Phys. Chem. Chem.*  
809 *Phys.* **2017**, *19*, 8282–8287.
- 810 (50) Zhang, Y.; Wang, Y.; Liao, P.; Wang, K.; Huang, Z.; Liu, J.;  
811 Chen, Q.; Jiang, J.; Wu, K. Detection and Manipulation of Charge  
812 States for Double-Decker DyPc2Molecules on Ultrathin CuO Films.  
813 *ACS Nano* **2018**, *12*, 2991–2997.
- 814 (51) Studniarek, M.; Wäckerlin, C.; Singha, A.; Baltic, R.; Diller, K.;  
815 Donati, F.; Rusponi, S.; Brune, H.; Lan, Y.; Klyatskaya, S.; Ruben, M.;  
816 Seitsonen, A. P.; Dreiser, J. Understanding the Superior Stability of  
817 Single-Molecule Magnets on an Oxide Film. *Adv. Sci.* **2019**, *6*,  
818 1901736.
- 819 (52) Hellerstedt, J.; Cahlik, A.; Švec, M.; de la Torre, B.; Moro-  
820 Lagares, M.; Chutora, T.; Papoušková, B.; Zoppellaro, G.; Mutombo,  
821 P.; Ruben, M.; Zbořil, R.; Jelinek, P. On-surface structural and  
822 electronic properties of spontaneously formed Tb2Pc3 single  
823 molecule magnets. *Nanoscale* **2018**, *10*, 15553–15563.
- 824 (53) Katoh, K.; Komeda, T.; Yamashita, M. The Frontier of  
825 Molecular Spintronics Based on Multiple-Decker Phthalocyaninato  
826 TbIII Single-Molecule Magnets. *Chem. Rec* **2016**, *16*, 987–1016.
- 827 (54) Schwöbel, J.; Fu, Y.; Brede, J.; Dilullo, A.; Hoffmann, G.;  
828 Klyatskaya, S.; Ruben, M.; Wiesendanger, R. Real-space observation  
of spin-split molecular orbitals of adsorbed single-molecule magnets. *829*  
*Nat. Commun.* **2012**, *3*, 953. 830
- (55) Wäckerlin, C.; Donati, F.; Singha, A.; Baltic, R.; Rusponi, S.;  
831 Diller, K.; Patthey, F.; Pivetta, M.; Lan, Y.; Klyatskaya, S.; Ruben, M.;  
832 Brune, H.; Dreiser, J. Giant Hysteresis of Single-Molecule Magnets  
833 Adsorbed on a Nonmagnetic Insulator. *Adv. Mater.* **2016**, *28*, 5195–  
834 5199. 835
- (56) Qi, Z. K.; Mishra, P.; Ara, F.; Oka, H.; Sainoo, Y.; Katoh, K.;  
836 Yamashita, M.; Komeda, T. Magnetic Hysteresis of Single-Molecule  
837 Magnets Adsorbed on Ferromagnetic Substrate. *ACS Nano* **2019**,  
838 DOI: 10.1021/acsnano.9b04428. 839
- (57) Granet, J.; Sicot, M.; Kierren, B.; Lamare, S.; Chérioux, F.;  
840 Baudelet, F.; Fagot-Revurat, Y.; Moreau, L.; Malterre, D. Tuning the  
841 Kondo resonance in two-dimensional lattices of cerium molecular  
842 complexes. *Nanoscale* **2018**, *10*, 9123–9132. 843
- (58) Ecija, D.; Auwärter, W.; Vijayaraghavan, S.; Seufert, K.;  
844 Bischoff, F.; Tashiro, K.; Barth, J. V. Assembly and manipulation of  
845 rotatable cerium porphyrinato sandwich complexes on a surface. *846*  
*Angew. Chem., Int. Ed.* **2011**, *50*, 3872–3877. 847
- (59) Urgel, J. I.; Ecija, D.; Vijayaraghavan, S.; Pörtner, M.; Bocquet,  
848 M.-L.; Auwärter, W.; Barth, J. V. In-Situ Growth of Gadolinium  
849 Phthalocyaninato Sandwich Complexes on the Ag(111) Surface. *850*  
*ChemPhysChem* **2019**, *20*, 2301–2304. 851
- (60) Diller, K.; Singha, A.; Pivetta, M.; Wäckerlin, C.; Hellwig, R.;  
852 Verdini, A.; Cossaro, A.; Floreano, L.; Velez-Fort, E.; Dreiser, J.;  
853 Rusponi, S.; Brune, H. Magnetic properties of on-surface synthesized  
854 single-ion molecular magnets. *RSC Adv.* **2019**, *9*, 34421–34429. 855
- (61) Marbach, H. Surface-Mediated in Situ Metalation of Porphyrins  
856 at the Solid-Vacuum Interface. *Acc. Chem. Res.* **2015**, *48*, 2649–2658. 857
- (62) Diller, K.; Papageorgiou, A. C.; Klappenberger, F.; Allegretti, F.;  
858 Barth, J. V.; Auwärter, W. In vacuo interfacial tetrapyrrole metallation.  
859 *Chem. Soc. Rev.* **2016**, *45*, 1629–1656. 860
- (63) Schöniger, M.; Kachel, S. R.; Herritsch, J.; Schröder, P.; Hutter,  
861 M.; Gottfried, J. M. Direct synthesis of dilithium tetraphenylporphyrin:  
862 in: facile reaction of a free-base porphyrin with vapor-deposited  
863 lithium. *Chem. Commun.* **2019**, *55*, 13665–13668. 864
- (64) Baklanov, A.; Garnica, M.; Robert, A.; Bocquet, M.-L.; Seufert,  
865 K.; Küchle, J. T.; Ryan, P. T. P.; Haag, F.; Kakavandi, R.; Allegretti, F.;  
866 Auwärter, W. On-Surface Synthesis of Nonmetal Porphyrins. *J. Am.*  
867 *Chem. Soc.* **2020**, *142*, 1871–1881. 868
- (65) Hu, J.; Strand, F. S.; Chellappan, R. K.; Zhang, Z.; Shen, K.;  
869 Hu, J.; Ji, G.; Huai, P.; Huang, H.; Wang, P.; Li, Z.; Jiang, Z.; Wells, J.  
870 W.; Song, F. Direct Synthesis of Semimetal Phthalocyanines on a  
871 Surface with Insights into Interfacial Properties. *J. Phys. Chem. C*  
872 **2020**, *124*, 8247–8256. 873
- (66) Bischoff, F.; Seufert, K.; Auwärter, W.; Seitsonen, A. P.; Heim,  
874 D.; Barth, J. V. Metalation of Porphyrins by Lanthanide Atoms at  
875 Interfaces: Direct Observation and Stimulation of Cerium Coordina-  
876 tion to 2H-TPP/Ag(111). *J. Phys. Chem. C* **2018**, *122*, 5083–5092. 877
- (67) Gottfried, J. M. Surface chemistry of porphyrins and  
878 phthalocyanines. *Surf. Sci. Rep.* **2015**, *70*, 259–379. 879
- (68) Auwärter, W.; Ecija, D.; Klappenberger, F.; Barth, J. V.  
880 Porphyrins at interfaces. *Nat. Chem.* **2015**, *7*, 105–120. 881
- (69) Dienel, T.; Gómez-Díaz, J.; Seitsonen, A. P.; Widmer, R.;  
882 Iannuzzi, M.; Radican, K.; Sachdev, H.; Müllen, K.; Hutter, J.;  
883 Gröning, O. Dehalogenation and Coupling of a Polycyclic Hydro-  
884 carbon on an Atomically Thin Insulator. *ACS Nano* **2014**, *8*, 6571–  
885 6579. 886
- (70) Morchutt, C.; Björk, J.; Krotzky, S.; Gutzler, R.; Kern, K.  
887 Covalent coupling via dehalogenation on Ni(111) supported boron  
888 nitride and graphene. *Chem. Commun.* **2015**, *51*, 2440–2443. 889
- (71) Urgel, J. I.; Schwarz, M.; Garnica, M.; Stassen, D.; Bonifazi, D.;  
890 Ecija, D.; Barth, J. V.; Auwärter, W. Controlling Coordination  
891 Reactions and Assembly on a Cu(111) Supported Boron Nitride  
892 Monolayer. *J. Am. Chem. Soc.* **2015**, *137*, 2420–2423. 893
- (72) Zhao, W.; Dong, L.; Huang, C.; Win, Z. M.; Lin, N. Cu- and  
894 Pd-catalyzed Ullmann reaction on a hexagonal boron nitride layer.  
895 *Chem. Commun.* **2016**, *52*, 13225–13228. 896

- 897 (73) Rizzo, D. J.; et al. Revealing the Local Electronic Structure of a  
898 Single-Layer Covalent Organic Framework through Electronic  
899 Decoupling. *Nano Lett.* **2020**, *20*, 963–970.
- 900 (74) Riss, A.; Richter, M.; Pérez Paz, A.; Wang, X.-Y.; Raju, R.; He,  
901 Y.; Ducke, J.; Corral, E.; Wuttke, M.; Seufert, K.; et al. Polycyclic  
902 aromatic chains on metals and insulating layers by repetitive [3 + 2]  
903 cycloadditions. *Nat. Commun.* **2020**, *11*, 1490.
- 904 (75) Joshi, S.; Ecija, D.; Koitz, R.; Iannuzzi, M.; Seitsonen, A. P.;  
905 Hutter, J.; Sachdev, H.; Vijayaraghavan, S.; Bischoff, F.; Seufert, K.;  
906 Barth, J. V.; Auwärter, W. Boron Nitride on Cu(111): An  
907 Electronically Corrugated Monolayer. *Nano Lett.* **2012**, *12*, 5821–  
908 5828.
- 909 (76) Kottas, G. S.; Clarke, L. I.; Horinek, D.; Michl, J. Artificial  
910 Molecular Rotors. *Chem. Rev.* **2005**, *105*, 1281–1376.
- 911 (77) Shannon, R. D. Revised effective ionic radii and systematic  
912 studies of interatomic distances in halides and chalcogenides. *Acta*  
913 *Crystallogr., Sect. A: Cryst. Phys., Diffr., Theor. Gen. Crystallogr.* **1976**,  
914 *32*, 751–767.
- 915 (78) Gottfried, J. M.; Flechtner, K.; Kretschmann, A.; Lukaszczuk, T.;  
916 Steinrück, H.-P. Direct Synthesis of a Metalloporphyrin Complex on a  
917 Surface. *J. Am. Chem. Soc.* **2006**, *128*, 5644–5645.
- 918 (79) Buchner, F.; Flechtner, K.; Bai, Y.; Zillner, E.; Kellner, I.;  
919 Steinrück, H.-P.; Marbach, H.; Gottfried, J. M. Coordination of Iron  
920 Atoms by Tetraphenylporphyrin Monolayers and Multilayers on  
921 Ag(111) and Formation of Iron-Tetraphenylporphyrin. *J. Phys. Chem.*  
922 *C* **2008**, *112*, 15458–15465.
- 923 (80) Di Santo, G.; Castellarin-Cudia, C.; Fanetti, M.; Taleatu, B.;  
924 Borghetti, P.; Sangaletti, L.; Floreano, L.; Magnano, E.; Bondino, F.;  
925 Goldoni, A. Conformational Adaptation and Electronic Structure of  
926 2H-Tetraphenylporphyrin on Ag(111) during Fe Metalation. *J. Phys.*  
927 *Chem. C* **2011**, *115*, 4155–4162.
- 928 (81) Duncan, D. A.; Deimel, P. S.; Wiengarten, A.; Paszkiewicz, M.;  
929 Casado Aguilar, P.; Acres, R. G.; Klappenberger, F.; Auwärter, W.;  
930 Seitsonen, A. P.; Barth, J. V.; Allegretti, F. Bottom-Up Fabrication of a  
931 Metal-Supported Oxo-Metal Porphyrin. *J. Phys. Chem. C* **2019**, *123*,  
932 31011–31025.
- 933 (82) Papageorgiou, A. C.; et al. Self-Terminating Protocol for an  
934 Interfacial Complexation Reaction in Vacuo by Metal-Organic  
935 Chemical Vapor Deposition. *ACS Nano* **2013**, *7*, 4520–4526.
- 936 (83) Fuggle, J. C.; Burr, A. F.; Watson, L. M.; Fabian, D. J.; Lang, W.  
937 X-ray photoelectron studies of thorium and uranium. *J. Phys. F: Met.*  
938 *Phys.* **1974**, *4*, 335–342.
- 939 (84) Cordero, B.; Gómez, V.; Platero-Prats, A. E.; Revés, M.;  
940 Echeverría, J.; Cremades, E.; Barragán, F.; Alvarez, S. Covalent radii  
941 revisited. *Dalton Trans.* **2008**, 2832–2838.
- 942 (85) Auwärter, W.; Seufert, K.; Bischoff, F.; Ecija, D.;  
943 Vijayaraghavan, S.; Joshi, S.; Klappenberger, F.; Samudrala, N.;  
944 Barth, J. V. A surface-anchored molecular four-level conductance  
945 switch based on single proton transfer. *Nat. Nanotechnol.* **2012**, *7*, 41.
- 946 (86) Auwärter, W.; Seufert, K.; Klappenberger, F.; Reichert, J.;  
947 Weber-Bargioni, A.; Verdini, A.; Cvetko, D.; Dell'Angela, M.;  
948 Floreano, L.; Cossaro, A.; Bavdek, G.; Morgante, A.; Seitsonen, A.  
949 P.; Barth, J. V. Site-specific electronic and geometric interface  
950 structure of Co-tetraphenyl-porphyrin layers on Ag(111). *Phys. Rev.*  
951 *B: Condens. Matter Mater. Phys.* **2010**, *81*, 245403.
- 952 (87) Komeda, T.; Isshiki, H.; Liu, J.; Zhang, Y.-F.; Lorente, N.;  
953 Katoh, K.; Breedlove, B. K.; Yamashita, M. Observation and electric  
954 current control of a local spin in a single-molecule magnet. *Nat.*  
955 *Commun.* **2011**, *2*, 217.
- 956 (88) Tanaka, H.; Ikeda, T.; Takeuchi, M.; Sada, K.; Shinkai, S.;  
957 Kawai, T. Molecular Rotation in Self-Assembled Multidecker  
958 Porphyrin Complexes. *ACS Nano* **2011**, *5*, 9575–9582.
- 959 (89) Ducke, J.; Riss, A.; Pérez Paz, A.; Seufert, K.; Schwarz, M.;  
960 Garnica, M.; Rubio, A.; Auwärter, W. Layered Insulator/Molecule/  
961 Metal Heterostructures with Molecular Functionality through  
962 Porphyrin Intercalation. *ACS Nano* **2018**, *12*, 2677–2684.
- 963 (90) Schulz, F.; Drost, R.; Hämäläinen, S. K.; Liljeroth, P.  
964 Templated Self-Assembly and Local Doping of Molecules on Epitaxial  
965 Hexagonal Boron Nitride. *ACS Nano* **2013**, *7*, 11121–11128.
- (91) Liu, L.; Diemel, T.; Widmer, R.; Gröning, O. Interplay between  
Energy-Level Position and Charging Effect of Manganese Phthalo-  
cyanines on an Atomically Thin Insulator. *ACS Nano* **2015**, *9*, 968  
10125–10132.
- (92) Joshi, S.; Bischoff, F.; Koitz, R.; Ecija, D.; Seufert, K.; Seitsonen,  
A. P.; Hutter, J.; Diller, K.; Urgel, J. I.; Sachdev, H.; Barth, J. V.;  
Auwärter, W. Control of Molecular Organization and Energy Level  
Alignment by an Electronically patterned Boron Nitride Template.  
*ACS Nano* **2014**, *8*, 430–442.
- (93) Herrera-Gomez, A.; Bravo-Sanchez, M.; Ceballos-Sanchez, O.;  
Vazquez-Lepe, M. O. Practical methods for background subtraction in  
photoemission spectra. *Surf. Interface Anal.* **2014**, *46*, 897–905.
- (94) Romberg, R.; Frigo, S.; Ogurtsov, A.; Feulner, P.; Menzel, D.  
Photon stimulated desorption of neutral hydrogen atoms from  
condensed water and ammonia by resonant O1s and N1s excitation:  
search for the signature of ultrafast bond breaking. *Surf. Sci.* **2000**,  
451, 116–123.
- (95) Nečas, D.; Klapetek, P. Gwyddion: an open-source software for  
SPM data analysis. *Cent. Eur. J. Phys.* **2012**, *10*, 181–188.
- (96) Nuñez Beyerle, M. d. C. Thorium on a Silver(111)-Surface:  
Electronic Properties and Reactivity. M.Sc. thesis, Technical  
University of Munich, 2017.
- (97) Blöchl, P. E. Projector augmented-wave method. *Phys. Rev. B:*  
*Condens. Matter Mater. Phys.* **1994**, *50*, 17953–17979.
- (98) Perdew, J. P.; Burke, K.; Ernzerhof, M. Generalized Gradient  
Approximation Made Simple. *Phys. Rev. Lett.* **1996**, *77*, 3865–3868.
- (99) Kresse, G.; Furthmüller, J. Efficient iterative schemes for ab  
initio total-energy calculations using a plane-wave basis set. *Phys. Rev.*  
*B: Condens. Matter Mater. Phys.* **1996**, *54*, 11169–11186.
- (100) Grimme, S.; Antony, J.; Ehrlich, S.; Krieg, H. A consistent and  
accurate ab initio parametrization of density functional dispersion  
correction (DFT-D) for the 94 elements H-Pu. *J. Chem. Phys.* **2010**,  
132, 154104.
- (101) Lorente, N.; Robles, R. STMpw. Zenodo: 2019; <https://zenodo.org/record/3581159> (accessed Dec. 17, 2019);  
DOI: 10.5281/zenodo.3581159.